International Journal of Mass Spectrometry 283 (2009) 191–199

Contents lists available at ScienceDirect

International Journal of Mass Spectrometry

journal homepage: www.elsevier.com/locate/ijms

# Freezing, fragmentation, and charge separation in sonic sprayed water droplets

Lloyd W. Zilch, Joshua T. Maze, John W. Smith, Martin F. Jarrold*

*Chemistry Department, Indiana University, 800 East Kirkwood Avenue, Bloomington, IN 47405, United States*

ARTICLE INFO

*Article history:*
Received 8 January 2009
Received in revised form 19 March 2009
Accepted 19 March 2009
Available online 6 April 2009

*Keywords:*
Water droplet
Sonic spray
Image charge detection

ABSTRACT

Water droplets are generated by sonic spray, transferred into vacuum through a capillary interface, and then passed through two image charge detectors separated by a drift region. The image charge detectors measure the charge and velocity of each droplet. For around 1% of the droplets, the charge changes significantly between the detectors. In some cases it increases, in others it decreases, and for some droplets the charge changes polarity. We attribute the charge changing behavior to fragmentation caused by freezing. Simulations indicate that the time required for a droplet to cool and freeze in vacuum depends on its size, and that droplets with radii of 1–2 μm have the right size to freeze between the two detectors. These sizes correspond to the smaller end of the distribution present in the experiment. When the charge on a droplet increases or changes polarity, fragmentation must be accompanied by charge separation where fragments carry away opposite charges. In some cases, two fission fragments were observed in the second charge detector. We show examples where the droplet breaks apart to give fragments of the same charge and opposite charges. The fragmentation and charge changing behavior found here is consistent with what has been found in the freezing of larger suspended and supported droplets.



## 1. Introduction

We recently reported a study of micron-sized water droplets generated by sonic spray, electrospray, and a vibrating orifice aerosol generator (VOAG) [1]. After formation, the droplets were transmitted into vacuum using a capillary interface where their charge and mass were determined by charge detection mass spectrometry [2–5]. In this approach, the charged droplet travels through a conducting cylinder, and the image charge is detected with a charge sensitive preamplifier. The amplitude of the signal is proportional to the charge, and the duration of the signal (the time it takes for a droplet to travel through the cylinder) provides the velocity. If the energy is known, the measured velocity can be used to determine $m/z$, which, along with the measured charge, provides a value for the mass of the droplet. Unfortunately, the energy is not well defined in these experiments.

Normally, the energy of an ion in vacuum is set by accelerating it through a known potential difference. However, the droplets are accelerated to several hundred m/s as they enter the vacuum chamber through the capillary interface [6], which leads to a large uncertainty in their kinetic energy. To overcome this problem, we developed an approach that employs two image charge detectors separated by a pulsed accelerator [7]. The charge and velocity are measured in the first detector, the droplet is accelerated through a known potential difference in the pulsed accelerator, and then the charge and velocity are measured in the second detector. The $m/z$ ratio is determined from both the change in the velocity between the two detectors and the potential difference in the pulsed accelerator.

In an alternative version of this approach, the droplets are accelerated and then decelerated through a symmetric triangular-shaped potential in a region between the two image charge detectors [1]. In this case, the $m/z$ ratio is determined from the time shift that occurs due to the accelerating/decelerating potential. The charge and velocity are measured in both detectors. The average velocity is used to predict the time it should take for the droplet to travel between the two detectors in the absence of the accelerating/decelerating potential. The difference between the predicted and measured time (with the accelerating/decelerating potential) is then used to determine the $m/z$ ratio.

For most of the droplets that we measured, the charge in the second detector was the same as in the first. But this was not true for all droplets. For a small fraction of the droplets, around 1%, the charges measured in the first and second detector differed by a significant amount. Some droplets seemed to lose charge, for some droplets the charge seemed to increase, and some droplets even seemed to reverse their charge (i.e., flip from positive to negative) as they travel through vacuum!

However, both the pulsed accelerator and the time shift region employed in these measurements used fine mesh grids, and it is possible that the charge changing events could result from collisions between the droplets and the grids. To rule out this possibility

* Corresponding author.
*E-mail address:* mfj@indiana.edu (M.F. Jarrold).

1387-3806/$ – see front matter © 2009 Elsevier B.V. All rights reserved.
doi:10.1016/j.ijms.2009.03.010

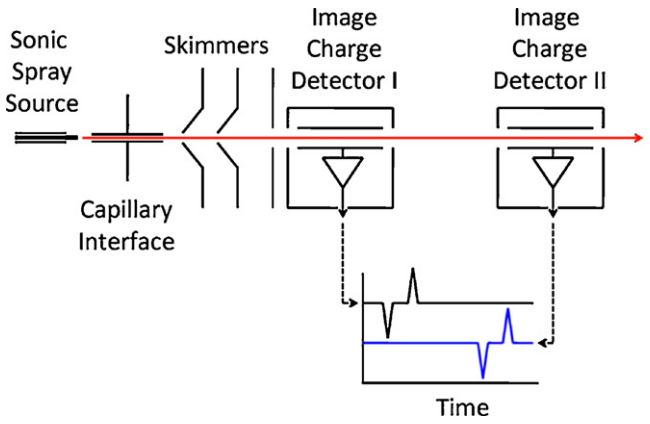


**Fig. 1.** Schematic diagram of the experimental apparatus. Charged drops, produced by a sonic spray source, enter the apparatus though a capillary interface. They pass through two differentially pumped skimmers and are detected by two image charge detectors separated by a drift region. The signals resulting from the two detectors are shown in the plot at the bottom of the figure.

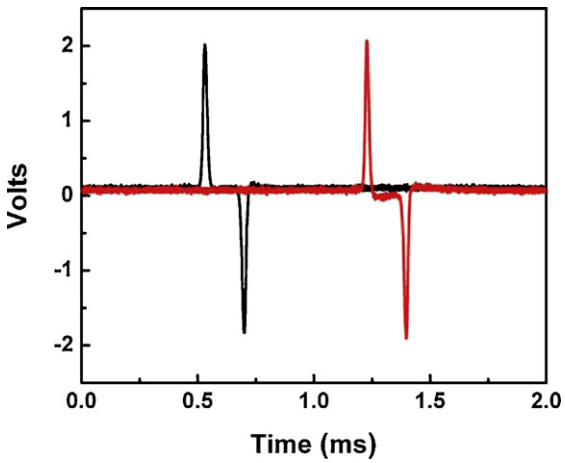


**Fig. 2.** The signal from a typical negatively charged droplet. The black trace is signal from the first detector and the red trace is from the second. The time between the positive and negative going peak in each trace is the flight time through the detector. The area under the peaks is proportional to the charge carried by the droplet. In this case the charge is the same in both detectors (within the expected uncertainty). (For interpretation of the references to color in this figure legend, the reader is referred to the web version of the article.)

we removed the pulsed accelerator and time shift regions so that there is a field-free drift region between the two detectors. The results of measurements performed with this configuration are reported here.

## 2. Experimental methods

A diagram schematic of the experimental apparatus is shown in Fig. 1 [1]. The apparatus consists of a sonic spray source, a capillary interface, and two differentially pumped skimmers, followed by two image charge detectors separated by a drift region. There are no grids in the path of the droplets in this configuration. All experiments were performed with HPLC grade water (Omni-Solv, Fisher Scientific) that was degassed prior to use by sonication under vacuum. The sonic spray source is modeled after the design Takats et al. [8]. It consists of two concentric fused silica capillaries (inner capillary: 100 μm ID and 200 μm OD; outer capillary: 250 μm ID and 350 μm OD; both from Polymicro Technologies, Phoenix, AZ). The inner capillary was supplied with water at 2–4 mL/h by a syringe pump. The outer capillary was fed with ultra high purity nitrogen (Airgas) at 400–800 kPa. The source was isolated from ground and not provided with a potential.

The droplets produced by the sonic spray source enter the instrument though a grounded stainless steel capillary (500 μm ID and 1.6 mm OD). The droplets pass through two grounded, differentially pumped skimmers and then enter the first image charge detector. The charge detectors are modeled after the design of Benner and coworkers [2]. They consist of a shielded stainless steel tube 3.15 cm in length, 0.65 cm ID, and 1.27 cm OD. A low-noise charge sensitive preamplifier (Amptek A250) with an external JFET (2SK152) is connected to the tube. When a charged droplet enters the cylinder, it induces an equal but opposite image charge. The output from the preamplifier is fed into a spectroscopy amplifier (Ortec, 571) where it is differentiated and then recorded by a 14-bit transient digitizer (AlazarTech, ATS460). After the droplets exit the first detector they fly through a 15 cm long field-free drift region and then enter the second charge detector. The signal from the second detector is processed in the same way as the first, and recorded in the second channel of the transient digitizer. Typically 10,000 transients are recorded in one run and then processed off-line. Everything in our instrument is grounded and there are no significant electric fields inside the vacuum chamber.

## 3. Results

The signals resulting from a typical droplet as it passes through both detectors are shown in Fig. 2. The black trace is the differentiated signal from the first image charge detector and the red trace is from the second. The first peak in both traces results from the droplet entering the detector, and the second peak is due to it leaving. The fact that the first peak is positive in both traces indicates that the droplet is negatively charged. For a positively charged droplet the first (entrance) peak is negative and the second (exit) peak is positive. The time difference between the positive and negative going peaks in each trace is the time it takes for the droplet to travel through the detector. Droplet velocities, determined from the flight time and the effective length of the detector, lie between 100 and 500 $m\,s^{-1}$. These velocities correspond to droplet kinetic energies in the GeV range (assuming an average mass of $1.2 \times 10^{-14}\,kg^{-1}$). All of the kinetic energy results from acceleration in the capillary interface.

The area under the peaks is proportional to the charge on the droplet. The proportionality constants were measured by putting a test charge onto the detection cylinders and measuring the system response. The test charge was obtained from a voltage pulse using a capacitor (seven 6.7 pF 1% capacitors connected in series) [7]. The accuracy of the calibration is limited by stray capacitance. Both detectors were calibrated in the same way. The calibration was cross-checked by plotting the charges recorded for a series of droplets in the second detector against the charge recorded in the first. Ideally, this plot should be a perfect straight line with a slope of one and an intercept of zero. In practice, we find there are some droplets where the charges differ by a substantial amount. These outliers are the subject of this paper. However, if they are removed, the rest of the points fall on a straight line with a slope indicating that the charges recorded in the two detectors agree to within 1%.

The transients from both detectors are first screened by a computer program which flags them if the background is not flat, if the transient contains the signal from more than one droplet, or if the charge determined from the negative and positive going peaks are not within a few percent of each other. Another computer program compares the signals in the two detectors. In some cases there is a droplet signal in the first detector but no signal in the second. Here, the droplet is lost between the two detectors: it may have broken-

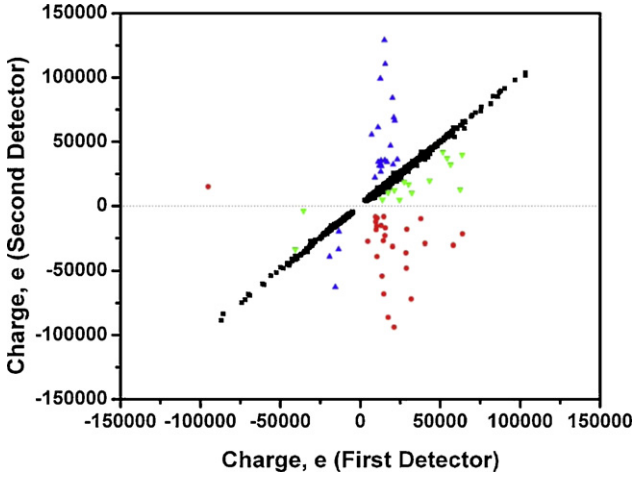


**Fig. 3.** The charge on a water droplet measured in the second detector plotted against the charge measured in the first. The majority of the droplets have similar charges in the both detectors (black squares). However, for some droplets the charge decreases (green triangles) or increases (blue triangles), and for some droplets the charge changes sign (red circles). (For interpretation of the references to color in this figure legend, the reader is referred to the web version of the article.)

up into many small fragments, or it may have a trajectory that misses the second detector (the second detector accepts a narrower range of angles than the first because it is further from the source). If there is a droplet signal in both transients, we do not automatically assume that the signals result from the same droplet. This becomes particularly important in situations where the charge measured in the two detectors is significantly different. In these cases, we require that the velocities measured in the two detectors agree to within narrow limits, and that the droplet arrives at the expected time in the second detector. Knowing the distance between the detectors and the velocity, we can predict precisely when the droplet should appear in the second transient. If the droplet signal from the second detector meets both of these criteria we assume that the signals in the first and second detector result from the same droplet.

Fig. 3 shows a plot of the charge determined for each droplet in the second detector versus the charge in the first. The majority of the droplets fall on a line with a slope of very close to one, indicating that the droplets have the same charge in both detectors (black squares in the figure). Roughly one percent of the points do not fall on the line, indicating that the charge measured in the two detectors is significantly different. For some droplets the charge decreases (green triangles), increases (blue triangles), or even changes sign (red circles).

Fig. 4 shows transients illustrating the three types of behavior mentioned above. The black lines show transients measured in the first detector and the red lines are measured in the second. Fig. 4(a) shows transients where the charge recorded in the second detector is smaller than in the first. In Fig. 4(b) the charge is larger (more positive) in the second detector, by approximately a factor of three. In Fig. 4(c) the droplet is positively charged in the first detector, and negatively charged in the second. In all cases the velocities measured in the first and second detectors agree within narrow limits and the signal in the second detector occurs at the expected time.

Fig. 5 shows examples of where fission fragments are observed in the second detector. In the first detector we detect a single droplet and in the second, the droplet has apparently broken-up into two fragments. Three examples are shown in the figure. In Fig. 5(a) a negative droplet apparently breaks apart into two fragment droplets with roughly equal charges. The sum of the charges on the two droplets found in the second detector is equal to the charge found on single droplet in the first detector. The velocities of the two droplets in the second detector are slightly different. One

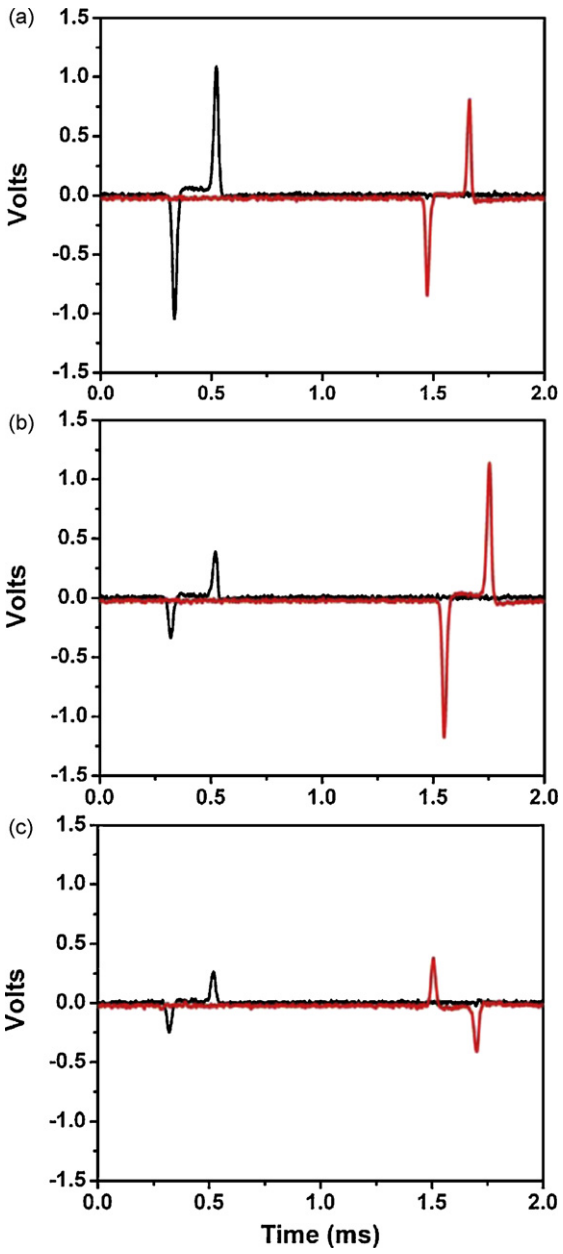


**Fig. 4.** Transients illustrating three types of "charge changing" behavior. The black line is the transient recorded in the first detector, and the red line is the transient recorded in the second. In (a) the positive charge recorded in the second detector is smaller than in the first. In (b) the positive charge increases. In (c) the droplet is positively charged in the first detector and negatively charged in the second. In all cases the velocities measured in the first and second detectors agree within narrow limits and the signal in the second detector occurs at the expected time. (For interpretation of the references to color in this figure legend, the reader is referred to the web version of the article.)

travels slightly faster, and the other slightly slower, than the parent droplet in the first detector. This difference in velocity (which results from the droplets' relative kinetic energy) is what allows us to detect the fragments in the second detector. Fig. 5(b) shows an asymmetric splitting event. A single positive droplet is observed in the first detector and two droplets, one with a large charge and one with a small charge, are found in the second detector. Again the sum of the charges in the second detector matches the charge found in the first. In both cases discussed above the charge on the progeny droplets is of the same polarity as the parent droplet. Fig. 5(c) shows an example where the progeny droplets have opposite charges. A single positive droplet in the first detector yields two droplets in

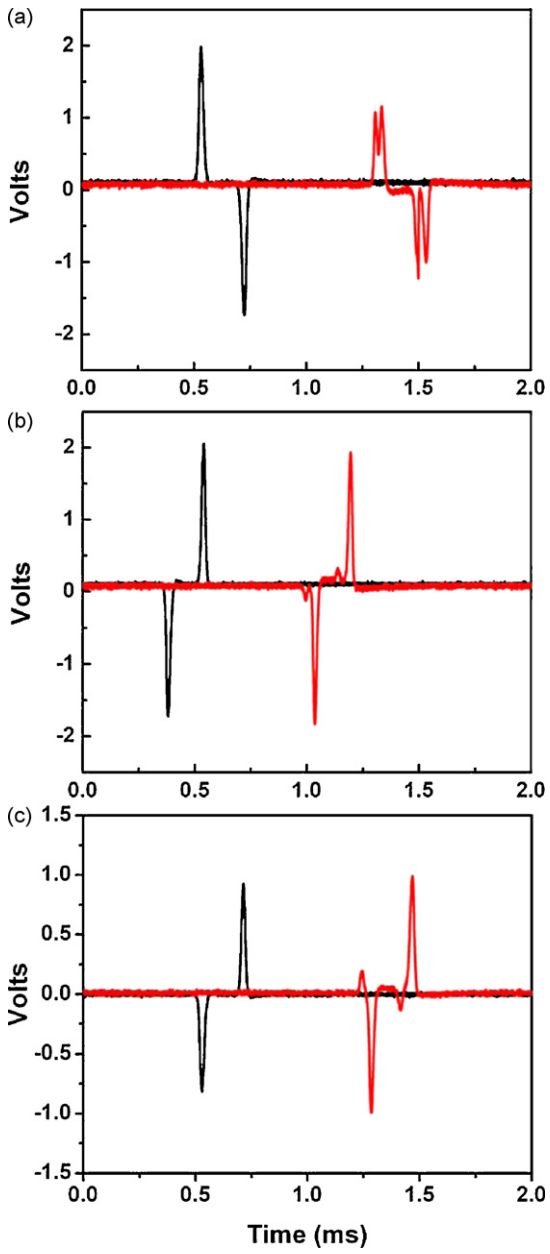


**Fig. 5.** Transients illustrating three types of droplet fission behavior. The black line is the transient recorded in the first detector, and the red line is the transient recorded in the second. In (a) a negatively charged droplet breaks up to give two negatively charged droplets with similar charges. In (b) a positively charged droplet undergoes an asymmetric fission to give two droplets; one with a high charge and the other with a low charge. In (c) a positively charged droplet breaks up to give a more highly charged positive droplet and a droplet with a small negative charge. (For interpretation of the references to color in this figure legend, the reader is referred to the web version of the article.)

the second; one is positively charged and the other is negatively charged. The positively charged droplet has a much larger charge than the negatively charged one. The sum of the charges on the negatively and positively charged droplets in the second detector equals the charge found on the droplet in the first detector.

## 4. Discussion

We start by considering possible explanations for why some of the droplets change their charge as they travel through vacuum.

Neutral water droplets are distorted by an electric field [9], and disrupted if the field exceeds the Taylor limit [10]. Charged droplets discharge at a lower field by jetting (emitting a stream of charged nanodroplets) [11]. Jetting can continue after the droplet is fully discharged, so that the droplet becomes charged with the opposite polarity. This provides a way to change the polarity of a charged droplet, but it requires a strong electric field. There is no electric field in the drift region of our experiment and so this cannot be the cause of the polarity changes that we observe.

In the absence of an electric field, droplets become unstable when their charge exceeds the Rayleigh limit (where electrostatic repulsion overcomes surface tension) [12,13]. Unstable droplets can fission or discharge by jetting [14–18]. Jetting has been observed for levitated microdroplets [14,15,18–20]. However, the charge on the sonic spray droplets studied here is substantially below the Rayleigh limit, and so electrostatically induced break-up of the droplets can be ruled out.

In previous work, we measured the size and charge of electrosprayed droplets transmitted through a capillary interface and found that they were charged to a small fraction of the Rayleigh limit (around 10% on average) [7]. More recent work has shown that the low charge results because the droplets are aerodynamically broken-up in the capillary interface by the air flow into the vacuum chamber [1]. A given flow velocity will reduce the droplets to a terminal size, in our case an average radius of around 2–3 μm. Droplets from both sonic spray and electrospray have about the same average size after transmission through the capillary interface, though the sonic spray droplets carry less charge and so they are even further from the Rayleigh limit than the electrospray droplets (i.e., less than 10%). Thus, electrostatic instability does not cause the droplets to break-up and so we seek another explanation for the break-up of the droplets as they travel between the detectors.

When the droplets enter the vacuum chamber they are evaporatively cooled, and if they are cooled to a sufficiently low temperature they may freeze. Perhaps the fragmentation and charge changing phenomena are caused by freezing. However, it only takes around a millisecond to travel between the detectors, can the droplets cool and freeze on this timescale? To answer this question we will estimate the cooling and freezing rates below.

Using microscopic reversibility [21], the rate constant for evaporation of a water molecule from a droplet of $n$ water molecules at temperature $T$ is given by

$$k(n,T) = k_c(n-1,T)\frac{P(n-1,T)}{k_B T} \quad (1)$$

where $k_c(n-1,T)$ is the collision rate between a water molecule and a droplet with $n-1$ water molecules at temperature $T$, $k_B$ is the Boltzmann constant, and $P_l(n-1,T)$ is the equilibrium vapor pressure above the liquid droplet. $P_l(n-1,T)$ is given by the Kelvin relationship

$$P_l(n-1,T) = P_{l,\infty}(T)\exp\left(\frac{2\sigma_l(T)M}{r(n,T)RT\rho_l(T)}\right) \quad (2)$$

where $P_{l,\infty}(T)$ is the vapor pressure above a flat liquid surface at temperature $T$, $\sigma_l(T)$ is the surface energy, $M$ is the molar mass, $r(n,T)$ is the droplet radius, and $\rho_l(T)$ is the density. $k_c(n-1,T)$ is given by

$$k_c(n-1,T) = \Omega N_A\left[\frac{8k_BT}{\pi\mu}\right]^{1/2} \quad (3)$$

where $N_A$ is the Avogadro constant, $\mu$ is the reduced mass, and $\Omega$ is the collision cross section for collisions between a water molecule and a droplet with $n-1$ water molecules. A geometric collision cross section is assumed where $\Omega = \pi[r(n-1,T) + r(H_2O)]^2$. The implementation of the equations described above requires

expressions for $\sigma_l(T)$, $P_{l,\infty}(T)$, and $\rho_l(T)$, which are given in Appendix A.

The average temperature change associated with the evaporation of one water molecule from the droplet is

$$\Delta T = \frac{L_l(n,T)}{C_l(n-1,T)} \tag{4}$$

where $L_{l,v}(n,T)$ is the latent heat (in J) for evaporation of a water molecule from a droplet with $n$ water molecules at temperature $T$, and $C_l(n-1,T)$ is the specific heat (in J K$^{-1}$) for a droplet with $n-1$ water molecules. Expressions for $L_{l,v}(n,T)$ and $C_l(n-1,T)$ are given in Appendix A.

We assume that freezing of the water droplets is limited by generation of a critical nucleus, and that once a critical nucleus is formed, freezing occurs on a time scale that is much shorter than the nucleation time. The nucleation mechanism for submicron water droplets has become controversial recently as Tabvazadeh and coworkers have challenged the existing paradigm of volume nucleation and suggested that surface nucleation is dominant [22,23]. However, no experimental study has been able to prove the importance of surface nucleation in submicron droplets [24]. For larger, micron-sized droplets homogeneous freezing rates are known to be proportional to the volume [25–27]. We assume volume nucleation here. The nucleation rates per unit volume per unit time were obtained from

$$J = A \exp\left(\frac{-\Delta G^*}{kT}\right) \tag{5}$$

where $\Delta G^*$ is the free energy barrier to formation of a critical nucleus. For the pre-exponential factor we use [28]

$$A = \frac{2(\sigma_{sl}(T)kT)^{1/2}}{v_m^{5/3}\eta(T)} \tag{6}$$

where $\sigma_{sl}(T)$ is the is the interfacial free energy per unit area of the boundary between solid and liquid, $\eta(T)$ is the liquid viscosity, and $v_m(T)$ is the molecular volume, $M/[\rho(T)N_A]$. Expressions for $\sigma_{sl}(T)$ and $\eta(T)$ are given in Appendix A. For $\Delta G^*$ we use

$$\Delta G^* = \frac{16\pi\sigma_{sl}^3}{3(\Delta G_v + w')^2} \tag{7}$$

where $\Delta G_v$ is the free energy change per unit volume for the transition from the old phase to the new, and $w'$ is the work associated with changing the surface area of the liquid outer phase due to the volume change as the solid nucleus forms in the interior of the droplet. $w'$ is given by

$$w' = \frac{2\sigma_l}{r(n,T)}\frac{\rho_l(T)-\rho_s(T)}{\rho_l(T)} \tag{8}$$

where $\rho_s(T)$ is the density of the solid phase at temperature $T$. An expression for $\rho_s(T)$ is given in Appendix A. $\Delta G_v$ is obtained from

$$\Delta G_v = -\frac{\Delta G_{fus}(T)\rho_l(T)}{M} \tag{9}$$

where $\Delta G_{fus}(T)$ is the molar free energy of fusion. An expression for $\Delta G_{fus}(T)$ is given in Appendix A.

The upper half of Fig. 6 shows a plot of temperature against time for water droplets with radii of 0.47 μm (black), 1.03 μm (red), 2.20 μm (green), and 4.74 μm (blue) (corresponding to $2\times10^{10}$, $2\times10^{11}$, $2\times10^{12}$, and $2\times10^{13}$ water molecules). The color-coded distributions at the bottom of the plot show when the droplets freeze according to the simulations. The solid lines show when the droplets start freezing (the nucleation time) and the dashed lines show when the droplet is completely frozen.

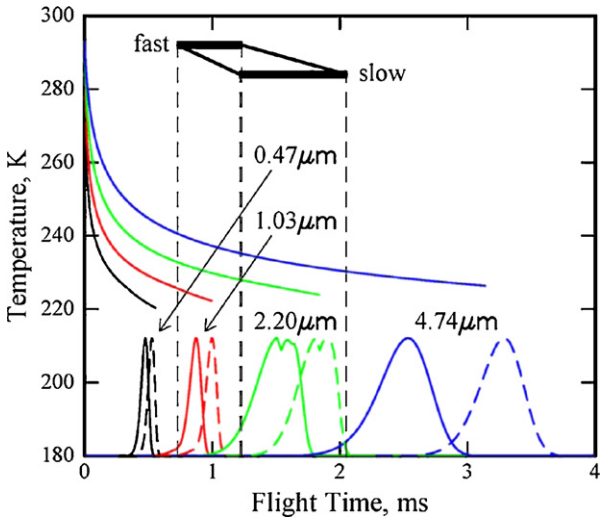


**Fig. 6.** Plot of temperature against time for droplets with radii of 0.47, 1.03, 2.20, and 4.74 μm. The distributions at the bottom of the plot show when the droplets first freeze (solid line) and completely freeze (dashed line). The thick horizontal bars and thin vertical dashed lines show the range of flight times that are sampled in the experiment (based on the measured velocity distribution).

In the simulations, larger droplets cool more slowly (because they have a smaller surface to volume ratio) and the smaller droplets freeze at a slightly lower temperature (because the nucleation rate, at a given temperature, is proportional to the volume). The average freezing temperatures are shown in Table 1, along with other information on the calculated freezing transitions. According to the simulations the droplets are deeply supercooled when they start freezing.

The droplets shrink as they evaporatively cool to an average of around 87–89% of their initial volume before they freeze (see Table 1). When they freeze, the latent heat is released. If the entire droplet were to freeze, the temperature would rise above the melting point. Instead, a fraction of the droplet freezes, and the temperature rises to the point where ice and liquid water coexist (presumably 273.15 K).

At 200 K supercooled water freezes into cubic ice, while at around 235 K a mixture of hexagonal and cubic ice is probably formed [29–31]. The cubic ice anneals into hexagonal ice at $T > 263$ K [29,30]. We assume that this annealing process is rapid enough at 273.15 K that all the cubic ice anneals into hexagonal ice before the temperature starts to drop again. The number of water molecules that initially freeze can then be determined from

$$n_{\text{freeze}} = \frac{\int_{T_{\text{freeze}}}^{273.15\,\text{K}} C_l(n',T)dT}{L_{l,s}(273.15\,\text{K})/N_A} \tag{10}$$

**Table 1**
Information about the calculated freezing transitions for droplets with initial radii of 0.47–4.74 μm.

| Initial droplet radius (μm) | Average time to initial freeze (ms) | Average $T$ at initial freeze (K) | Droplet size at initial freeze (vol%) | Fraction of ice after initial freeze | Average time to complete freeze (ms) | Droplet size at complete freeze (vol%) |
|---|---|---|---|---|---|---|
| 0.47 | 0.46 | 222.2 | 87.8 | 0.744 | 0.52 | 85.4 |
| 1.03 | 0.85 | 224.0 | 88.1 | 0.716 | 0.97 | 85.5 |
| 2.20 | 1.47 | 226.3 | 88.5 | 0.678 | 1.78 | 85.5 |
| 4.74 | 2.46 | 228.6 | 89.0 | 0.635 | 3.23 | 85.6 |

where $L_{l,s}$(273.15 K) is the latent heat for freezing at 273.15 K (6110 J mol$^{-1}$), $C_l(n',T)$ is the specific heat of the droplet (in J K$^{-1}$), and the integral runs from the temperature where the droplets start to freeze, $T_{freeze}$, to the normal melting point, 273.15 K. The fraction of the droplet that freezes can be determined from $n_{freeze}$ and the number of water molecules remaining in the droplet, $n'$. The average fractions that initially freeze are shown in Table 1. They range for 0.744 for the 0.47 μm diameter droplet to 0.635 for the 4.74 μm diameter droplet.

The partially frozen droplet will undergo further evaporative cooling, but the temperature will remain at around 273.15 K until the entire droplet freezes, and then the temperature of the frozen droplet will start decreasing again. The dashed lines at the bottom of Fig. 6 show the time distributions for when the droplets are completely frozen. The average times required for the droplet to completely freeze are also given in Table 1. The additional time required to completely freeze the droplet is a fraction of the nucleation time. By the time the droplet is completely frozen its radius has decreased to around 85% of its initial value (see Table 1).

The thick horizontal bars at the top of Fig. 6 show the range of flight times that are sampled in our experiment (based on the measured velocity distribution of the droplets, the distances from the end of the capillary interface to the first image charge detector, and the distance between the image charge detectors). The bars show the time spent traveling between the detectors for fast and slow moving droplets (the fast and slow velocities are the values at half the peak maximum in the velocity distribution [1]).

Even the fast moving droplets with radii around 0.47 μm are frozen before entering the first detector, and most of the droplets with radii around 4.74 μm remain liquid after passage through both detectors. Droplets with radii between these extremes freeze to a varying extent as they travel between the detectors. Fast moving droplets with radii around 1.03 μm freeze between the detectors, but the slow moving droplets of this size freeze before they enter the first detector. On the other hand, slow moving droplets with radii around 2.20 μm freeze between the detectors, but most of the fast moving droplets of this size remain liquid as they pass through the second detector. Overall, droplets with radii around 1–2 μm have the optimum size to freeze between the detectors.

We have measured the size distribution for electrospray droplet [7], but we have not been able to measure it for sonic spray because the sonic spray droplets carry less charge and have $m/z$ ratios beyond what we can reliably measure [1]. However, our results indicate that the average sizes for sonic spray and electrospray droplets are about the same. As noted above, the droplets are broken-up aerodynamically in the capillary interface until they are reduced to a terminal size [1], and so the droplet size distributions for electrospray and sonic spray should be similar. Fig. 7 shows the size distribution measured for electrosprayed droplets [7]. The distribution has a threshold at a radius of around 0.5 μm, peaks between 1 and 2 μm, and then tails-off to approach zero at around 5 μm. According to the simulations described above, droplets with radii around 1–2 μm have the optimum size to freeze between the detectors. This corresponds to the peak of the distribution shown in Fig. 7. The fact that optimum droplet size range from the simulations for freezing between the detectors falls inside the measured size distribution supports the idea that the charge changing and fragmentation phenomena results from freezing.

There has been a lot of interest in the freezing of water droplets because of its importance in the atmosphere and potential role in thunderstorms. A number of studies have focused on the fragmentation that can accompany freezing [32–36]. Fragmentation includes both the ejection of ice particles or splinters from a freezing drop and the shattering of a freezing drop (where it breaks up into several large pieces). In some cases the splinters result from spikes; sharp protuberances that grow out from the surface of the droplet as it freezes. Environmental factors strongly influence the fragmentation [37,38]. For example, dissolved gases (air and $CO_2$) promote shattering. Droplets that freeze in air under equilibrium conditions were not observed to shatter and only some ejected an ice splinter. In addition to fragmentation, freezing water droplets have been observed to eject microdroplets [39,40]. The studies mentioned above focused mainly on larger droplets than are studied here, but they are consistent with our observations.

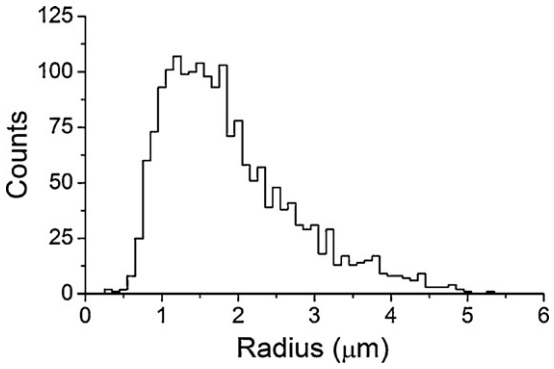


**Fig. 7.** Droplet size distribution for electrospray droplets (adapted from Ref. [7]).

In our experiments the ice particles are expected to fragment to relieve the strain generated by freezing under non-equilibrium conditions. Here is one scenario by which this may occur. After nucleation and the initial fast freezing event (where around 70% of the droplet freezes) the droplet is expected to consist of an ice shell surrounded by a liquid core (because the surface is being evaporatively cooled). As the remaining liquid water core freezes, the volume change that occurs on freezing will place the shell under a lot of stress. The resulting strain can be relieved by the shattering the ice shell, generating ice fragments and possibly a jet of water from the remaining liquid core.

It has been known for some time that a potential difference is generated across a water–ice interface during freezing. Studies of dilute solutions show that this is due to a differing propensity to trap ions in the freezing ice [41]. It is a transient effect, the potential difference dissipates when the ice stops freezing (because ice is a semiconductor). A temperature gradient across ice will also generate a potential difference (due to the different mobilities of $H^+$ and $OH^-$) with the colder ice becoming positively charged and the warmer ice negatively charged [42,43]. Thus it is not surprising that charge separation occurs when the freezing droplets fragment and that many of the splinters are strongly charged [34,44]. The ejection of charged ice splinters has also been observed during the generation of frost [45] and rime [46] (an accumulation of granular ice from a supercooled fog or cloud).

What is the polarity of the charge carried by the ejected fragments, and hence what charge is left behind? There is not a clear answer to this question. According to Mason and Maybank the splinters are usually positively charged [34]. However, Iribarne and collaborators found that about half the freezing droplets acquired a positive charge and half a negative charge [44]. Rydock and Williams found that the ice fragments ejected from a frost surface growing in a warm moist environment are systematically negatively charged [45]. They also reported that the magnitude of the charge is a strong function of the temperature.

We now consider the charge separation that occurs when the droplets fragment in our experiments. The initial charge on the sonic spray droplets is relatively low (less than 10% of the Rayleigh

limit), so a fragmentation process that increases the overall charge is not unreasonable. There are two ways that the charge can be distributed when the freezing droplets fragment:

(1) The fragments have the same polarity (i.e., there is no additional charge separation in the fragmentation). In this case the charge on the parent droplet is shared among the progeny, and the sum of the charges on the progeny equals the charge on the parent. The charge on each fragment is always less than on the parent.
(2) The fragments have different polarities. Additional charge separation occurs in the fragmentation to give fragments with different polarities. The sum of the charges on the progeny equals the charge on the parent, but the absolute charge for the progeny, $\sum(q_i^2)^{1/2}$, is larger than for the parent. The charge on the individual progeny can be larger than on the parent or have the opposite polarity to the parent. If only two progeny are generated one will have a larger charge than the parent and the other will have a charge of the opposite polarity.

Consider a droplet that breaks apart into two roughly equal fragments. The fragments will separate as they travel through our apparatus. There are two extremes. If they separate along a vector that is parallel to their movement through the apparatus we will see two signals in the second detector with one fragment (the first one to arrive) having a velocity that is slightly larger than in the first detector, and the other having a velocity which is slightly slower. An example of this behavior is shown in Fig. 5(a). In situations where the fragments separate along a vector that is perpendicular to their trajectory through the apparatus, both fragments will reach the second detector at the same time and the fragmentation will be hidden. It is possible that one of the fragments will be lost because it misses the second detector. The angular acceptance of the second detector is smaller than the first and in the absence of fragmentation a significant fraction of the droplets are "lost" (present in the first detector but not in the second).

Loss of one of the fragments could account for the transients shown in Fig. 4 where we see only a single droplet signal in both detectors, but the charge apparently changes. The other fragment (or fragments) necessary to conserve the charge in these traces could be lost. For example, consider Fig. 4(a), a positive droplet signal is observed from both detectors and the signal in the second detector is smaller than in the first. Another positively charged droplet required to conserve the charge, must be lost. Alternatively, this behavior could also result from the generation of a large number of small fragments, each one with a charge that it too small to be picked up by the second detector. For Fig. 4(b) a single positively charged droplet is observed in both detectors but the charge in the second detector is substantially larger than in the first. An increase in the charge like this requires charge separation in the fragmentation process. To conserve the overall charge, a negatively charged fragment must be generated. This fragment must be lost between the detectors or the negative charge must be distributed over many small fragments so that the charge on each one is too small to detect. Finally, for Fig. 4(c) a positive droplet signal is observed in the first detector and a negative droplet signal is found in the second. This also requires charge separation in the fragmentation process. Charge conservation requires that a positively charged droplet is formed and lost between the detectors.

While the charge changing and fragmentation behavior is consistent with freezing being the origin, we briefly mention another possible explanation here: that the fragmentation events result from the decay of binary orbiting pairs of oppositely charged droplets. In this scenario, the droplet pairs are held in orbit by a balance of attractive electrostatic and repulsive centrifugal interactions, in a way analogous to binary stars (where gravity replaces the electrostatic interactions). A combination of evaporation and the transfer of charge between the orbiting pair, causes the pair to collapse and/or fly apart. While there is clear precedent for the fracture/freezing explanation described above, we cannot completely rule-out the binary orbiting pair explanation, and this could be responsible for some of the charge changing events that we have observed.

## 5. Conclusion

The charge changing and fragmentation behavior observed for some sonic spray droplets is mainly attributed to freezing. Simulations show that the timescale for evaporative cooling and freezing of the resulting supercooled droplets depends on the droplet size. Droplets with radii of 1–2 μm have the right size to freeze between the detectors in our experiment. Droplets of this size range are on the low end of the distribution present in the experiment (0.5–5.0 μm). The observation that some fragments have a larger charge than the parent or that the polarity changes, indicates that charge separation occurs during the fragmentation of the freezing droplets. The charge changing and fragmentation behavior observed here is consistent with studies of the fragmentation and shattering of larger suspended and supported droplets.

## Acknowledgment

This work was partially supported by a grant from the METACyt Initiative, Indiana University.

## Appendix A

For the surface energy of liquid water $\sigma_l(T)$ (in J m$^{-2}$) we use [47]

$$\sigma_l(T) = 111.63 - 0.13167T \tag{11}$$

for the vapor pressure over a flat liquid water surface $P_{l,\infty}(T)$ (in Pa) we use [48]

$$\ln(P_{l,\infty}(T)) = 54.842763 - \frac{6763.22}{T} - 4.210\ln T + 0.000367T + \tanh\{0.0415(T-218.8)\}\left(53.878 - \frac{1331.22}{T} - 9.44523\ln T + 0.014025T\right) \tag{12}$$

and for the density of liquid water $\rho_l(T)$ (in g cm$^{-3}$) we use [49]

$$V(T) = [1 - f_{II}(T)]V_I(T) + f_{II}(T)V_{II}(T) \tag{13}$$

where

$$\begin{aligned} V_I(T) &= 1.08761[1 + 4.78005\times10^{-4}(T-225.334)] \\ V_{II}(T) &= 0.84632[1 + 1.29473\times10^{-3}(T-225.334)] \end{aligned} \tag{14}$$

and

$$f_{II}(T) = \tanh\left[\frac{4.54866\times10^{-2}(T-225.334) + (3.6522\times10^{-4}(T-225.334))^2}{1 + 8.69196\times10^{-2}(T-225.334)}\right] \tag{15}$$

for $T > 225.334$ K and $f_{II}(T) = 0$ for $T < 225.224$ K. The latent heat for evaporation from a liquid droplet $L_{l,v}(n,T)$ (in J) is obtained from

$$L_{l,v}(n,T) = \frac{57635.5 - 46.256T}{N_A} - \frac{2\sigma(T)M}{r(n,T)\rho_l(T)} \tag{16}$$

where the first term is the latent heat of evaporation from bulk water and the second term accounts for the change in the surface

energy for a small droplet. The specific heat for a droplet with $n-1$ water molecules $C_l(n-1,T)$ (in J K$^{-1}$) is obtained from [47]

$$C_l(n-1,T) = \frac{n-1}{N_A}\left(72.92 + 0.01896(T-226.0) + \frac{41.7}{0.0072(T-226)^2}\right) \quad (17)$$

for $T \geq 226$ K, and

$$C_l(n-1,T) = \frac{n-1}{N_A}(3.990 + 0.3220T - 0.0003608T^2) \quad (18)$$

for $T < 226$ K. For $\sigma_{sl}(T)$ (in J m$^{-2}$) we use

$$\sigma_{sl}(T) = 20.6 \times 10^{-3}\left(\frac{200.0}{T}\right)^{0.8566} \quad (19)$$

and for $\eta(T)$ (in Pa s)

$$\eta(T) = \exp(104.22 - 1.0377T + 0.0032822T^2 - 3.531 \times 10^{-6}T^3) \quad (20)$$

The later equation was obtained by fitting viscosities measured in the 249–313 K temperature range [50,51]. Hence we extrapolate into the relevant temperature range, which is where the droplets freeze (220–235 K according to these simulations). The equation for $\sigma_{sl}(T)$ was obtained by fitting the nucleation rates measured by Wood and Walton [52] at around 237 K for droplets 3–26 μm in diameter, and those measured by Huang and Bartell [47] at around 200 K for droplets 6–7 nm in diameter. These values bracket the relevant temperature range. However, it seems that at 200 K supercooled water freezes into cubic ice, while at around 237 K a mixture of hexagonal and cubic ice is probably formed [29,30]. The $\sigma_{sl}(T)$ values we deduced from fitting the nucleation rates at around 200 and 237 K were slightly different to those found by Huang and Bartell, we assume that this is due to the use of different values for $\eta(T)$.

The density of ice, $\rho_s(T)$, is obtained from

$$\rho_s(T) = 0.9404 - 9.2597 \times 10^{-5}T + 3.8111 \times 10^{-7}T^2 - 1.3103 \times 10^{-9}T^3 \quad (21)$$

which was derived by fitting the measured densities of hexagonal ice [53] (the densities of hexagonal and cubic ice are almost identical). The molar free energy of fusion, $\Delta G_{fus}(T)$, (in J mol$^{-1}$) is obtained from [47]

$$\Delta G_{fus}(T) = -2007 + 37.163T - 0.1102T^2 \quad (22)$$

for $T \geq 226$ K, and

$$\Delta G_{fus}(T) = 1139.5 + 13.016T - 0.06499T^2 \quad (23)$$

for $T < 226$ K.

## References


[1] L.W. Zilch, J.T. Maze, J.W. Smith, G.E. Ewing, M.F. Jarrold, Charge separation in the aerodynamic break-up of micrometer-sized water droplets, J. Phys. Chem. A 112 (2008) 13352–13363.
[2] S.D. Fuerstenau, W.H. Benner, Molecular weight determination of megadalton DNA electrospray ions using charge detection time-of-flight mass spectrometry, Rapid Commun. Mass Spectrom. 9 (1995) 1528–1538.
[3] J.C. Schultz, C.A. Hack, W.H. Benner, Mass determination of megadalton-DNA electrospray ions using charge detection mass spectrometry, J. Am. Soc. Mass Spectrom. 9 (1998) 305–313.
[4] J.C. Schultz, C.A. Hack, W.H. Benner, Polymerase chain reaction products analyzed by charge detection mass spectrometry, Rapid Commun. Mass Spectrom. 13 (1999) 15–20.
[5] S.D. Fuerstenau, W.H. Benner, J.J. Thomas, C. Brugidou, B. Bothner, G. Siuzdak, Mass spectrometry of an intact virus, Angew. Chem. Int. Ed. 40 (2001) 541–544.
[6] J.T. Maze, T.C. Jones, M.F. Jarrold, Negative droplets from positive electrospray, J. Phys. Chem. A 110 (2006) 12607–12612.
[7] S.R. Mabbett, L.W. Zilch, J.T. Maze, J.W. Smith, M.F. Jarrold, Pulsed acceleration charge detection mass spectrometry, Anal. Chem. 79 (2007) 8431–8439.
[8] Z. Takats, S.C. Nanita, R.G. Cooks, G. Schlosser, K. Vekey, Amino acid clusters formed by sonic spray ionization, Anal. Chem. 75 (2003) 1514–1523.
[9] W.A. Macky, Some investigations of the deformation and breaking of water drops in strong electric fields, Proc. R. Soc. Lond. A 133 (1931) 565–587.
[10] G. Taylor, Disintegration of water droplets in an electric field, Proc. R. Soc. Lond. A 280 (1964) 383–397.
[11] R.L. Grimm, J.L. Beauchamp, Dynamics of field-induced droplet ionization: time resolved studies of distortion, jetting, and progeny formation from charged and neutral methanol droplets exposed to strong electric fields, J. Phys. Chem. B 109 (2005) 8244–8250.
[12] Rayleigh Lord, On the equilibrium of liquid conducting masses charged with electricity, Philos. Mag. 14 (1882) 184–186.
[13] C.D. Hendricks, J.M. Schneider, Stability of a conducting droplet under the influence of surface tension and electrostatic forces, Am. J. Phys. 31 (1963) 450–453.
[14] D.C. Taflin, T.L. Ward, E.J. Davis, Electrified droplet fission and the Rayleigh Limit, Langmuir 5 (1989) 376–384.
[15] A. Gomez, K. Tang, Charge fission of droplets in electrostatic sprays, Phys. Fluids 6 (1994) 404–414.
[16] X. Feng, M.J. Bogan, G.R. Agnes, Coulomb fission event resolved progeny droplet production from isolated evaporating methanol droplets, Anal. Chem. 73 (2001) 4499–4507.
[17] J.N. Smith, R.C. Flagan, J.L. Beauchamp, Droplet evaporation and discharge dynamics in electrospray ionization, J. Phys. Chem. A 106 (2002) 9957–9967.
[18] D. Duft, T. Achtzehn, R. Muller, B.A. Huber, T. Leisner, Coulomb fission—Rayleigh jets from levitated microdroplets, Nature 421 (2003) 128–1128.
[19] D.B. Hager, N.J. Dovichi, Behavior of microscopic liquid droplets near a strong electrostatic field, droplet electrospray, Anal. Chem. 66 (1994) 1593–1594.
[20] D.B. Hager, N.J. Dovichi, J.S. Klassen, P. Kebarle, Droplet electrospray mass spectrometry, Anal. Chem. 66 (1994) 3944–3949.
[21] C.E. Klots, Evaporative cooling, J. Chem. Phys. 83 (1985) 5854–5860.
[22] A. Tabazadeh, Y.S. Djikaev, P. Hamill, H. Reiss, Laboratory evidence for surface nucleation of solid polar stratospheric cloud particles, J. Phys. Chem. A 106 (2002) 10238–10246.
[23] A. Tabazadeh, Y.S. Djikaev, H. Reiss, Surface crystallization of supercooled water in clouds, Proc. Natl. Acad. Sci. U.S.A. 99 (2002) 15873–15878.
[24] Ó. Sigurbjönrsson, R. Signorell, Volume versus surface nucleation in freezing aerosols, Phys. Rev. E 77 (2008) 051601.
[25] D. Duft, T. Leisner, Laboratory evidence for volume-dominated nucleation of ice in supercooled water microdroplets, Atmos. Chem. Phys. 4 (2004) 1997–2000.
[26] P. Stöckel, I.M. Weidinger, H. Baumgärtel, T. Leisner, Rates of homogeneous ice nucleation in levitated $H_2O$ and $D_2O$ droplets, J. Phys. Chem. A 109 (2005) 2540–2546.
[27] S.E. Wood, M.B. Baker, B.D. Swanson, Instrument for studies of homogeneous and heterogeneous ice nucleation in free-falling supercooled water droplets, Rev. Sci. Inst. 73 (2002) 3988–3996.
[28] L.S. Bartell, T.S. Dibble, Electron diffraction studies of the kinetics of phase changes in molecular clusters. Freezing of $CCl_4$ in supersonic flow, J. Phys. Chem. 95 (1991) 1159–1167.
[29] B.J. Murray, D.A. Knopf, A.K. Bertram, The formation of cubic ice under conditions relevant to the earth's atmosphere, Nature 434 (2005) 202–205.
[30] B.J. Murray, A.K. Bertram, Formation and stability of cubic ice in water droplets, Phys. Chem. Chem. Phys. 8 (2006) 186–192.
[31] G.P. Johari, On the coexistence of cubic and hexagonal ice between 160 K and 240 K, Philos. Mag. B 78 (1978) 375–383.
[32] V.J. Schaefer, Formation of ice crystals in ordinary and nuclei free air, Ind. Eng. Chem. 44 (1952) 1300–1304.
[33] E.J. Langham, B.J. Mason, The heterogeneous and homogeneous nucleation of supercooled water, Proc. R. Soc. Lond. A 247 (1958) 493–504.
[34] B.J. Mason, J. Maybank, The fragmentation and electrification of freezing water drops, Q. J. R. Meteorol. Soc. 86 (1960) 176–185.
[35] L.G. Kachurin, V.I. Bekryaev, Investigation of the electrification of crystallizing water, Dokl. Akad. Nauk. S.S.S.R. 130 (1960) 57–60.
[36] J. Latham, B.J. Mason, Generation of electrical charge associated with formation of soft hail in thunderclouds, Proc. R. Soc. Lond. A 260 (1961) 537–549.
[37] J.E. Dye, P.V. Hobbs, Influence of environmental parameters on freezing and fragmentation of suspended water drops, J. Atmos. Sci. 25 (1967) 82–96.
[38] D.A. Johnson, J. Hallett, Freezing, Shattering of supercooled water drops, Q. J. R. Meteorol. Soc. 94 (1968) 468–482.
[39] R.J. Cheng, Water drop freezing—ejection of microdroplets, Science 170 (1970) 1395–1396.
[40] P.V. Hobbs, Microdroplets and water drop freezing, Science 173 (1971) 849–850.
[41] J.E. Workman, S.E. Reynolds, Electrical phenomena occurring during the freezing of dilute aqueous solutions and their possible relationship to thunderstorm electricity, Phys. Rev. 78 (1950) 254–260.
[42] J. Lantham, B.J. Mason, Electrical charge transfer associated with temperature gradients in ice, Proc. R. Soc. Lond. A 2260 (1961) 523–536.
[43] J. Latham, C.D. Stow, Electrification associated with the evaporation of ice, J. Atmos. Sci. 22 (1965) 320–324.
[44] R.J. Kolomeychuk, D.C. McKay, J.V. Iribarne, The fragmentation and electrification of freezing drops, J. Atmos. Sci. 32 (1975) 974–979.
[45] J.P. Rydock, E.R. Williams, Charge separation associated with frost growth, Q. J. R. Meteorol. Soc. 117 (1991) 409–420.

[46] E.E. Avila, G.S. Longo, R.E. Burgesser, Mechanism for electric charge separation by ejection of charged particles from an ice particle growing by riming, Atmos. Res. 69 (2003) 99–108.
[47] J. Huang, L.S. Bartell, Kinetics of homogenous nucleation in freezing of large water clusters, J. Phys. Chem. 99 (1995) 3924–3931.
[48] D.M. Murphy, T. Koop, Review of the vapor pressures of ice and supercooled water for atmospheric applications, Q. J. R. Meteorol. Soc. 131 (2005) 1539–1565.
[49] M. Vedamuthu, S. Singh, G.W. Robinson, Properties of liquid water: origin of the density anomalies, J. Phys. Chem. 98 (1994) 2222–2230.
[50] J. Hallett, The temperature dependence of the viscosity of supercooled water, Proc. Phys. Soc. Lond. 82 (1963) 1046–1050.
[51] L.D. Eicher, B.J. Zwolinski, High-precision viscosity of supercooled water and analysis of the extended range temperature coefficient, J. Phys. Chem. 75 (1971) 2016–2024.
[52] G.R. Wood, A.G. Walton, Homogenous nucleation kinetics of ice from water, J. Appl. Phys. 41 (1970) 3027–3036.
[53] D.R. Lide (Ed.), Handbook of Chemistry and Physics, 87th edition, 2006–2007, Web Version: http://hbcpnetbase.com/, accessed 9/16/2006.